Journal of Power Sources 205 (2012) 394–401

Contents lists available at SciVerse ScienceDirect

Journal of Power Sources

journal homepage: www.elsevier.com/locate/jpowsour

Synthesis and electrode characteristics of solid solution $LiMn_{1-x}Fe_xPO_4(OH)$ $(0 \le x \le 0.3)$ with tavorite structure for lithium batteries

Yang Yang, Masaaki Hirayama, Kei Kubota, Ryoji Kanno*

Department of Electronic Chemistry, Interdisciplinary Graduate School of Science and Engineering, Tokyo Institute of Technology, 4259 Nagatsuta, Midori-ku, Yokohama 226-8502, Japan

ARTICLE INFO

Article history:
Received 19 November 2011
Received in revised form
19 December 2011
Accepted 19 December 2011
Available online 29 December 2011

Keywords:
Lithium manganese hydroxyphosphate
Cathode material
Lithium batteries

ABSTRACT

A single phase of $LiMn_{1-x}Fe_xPO_4(OH)$ with the tavorite structure is synthesized by a H^+/Li^+ exchange reaction of $Mn_{1-x}Fe_xPO_4{\cdot}H_2O$ precursors and $LiNO_3$ in the composition range $0 \le x \le 0.3$. The materials are characterized by X-ray diffraction, thermogravimetry–differential thermal analysis, scanning electron microscopy, and charge–discharge measurements. Rietveld refinement results of synchrotron X-ray powder diffraction data reveal that $LiMn_{1-x}Fe_xPO_4(OH)$ forms a continuous solid solution over the entire composition range with a triclinic structure (space group: $P\bar{1}$). A linear reduction in the unit cell dimensions a and b and a linear increase in the cell parameter c are accompanied by a local change in the bonding geometry of $M^{3+}O_6$ and LiO_6 octahedra with increasing iron content. Iron-substituted phases exhibit an improved charge–discharge performance with a 30% increase in capacity for voltages in the range of 2.0–4.6 V as the iron content increases from $x = 0.0$ to 0.3. The improved electrochemical properties and thermal stability reveal a correlation with distortion relaxation in the local geometry caused by partial substitution of Mn^{3+} by Fe^{3+} in $LiMnPO_4(OH)$.

1. Introduction

Lithium batteries are currently the most advanced means to store electrical energy as they have extremely high energy densities. However, their application is mainly limited to compact mobile devices due to cost and safety problems. Novel polyanionic electrode materials containing phosphate units have been attracting great interest, since discovery of the $LiFePO_4$ materials, which shows good electrochemical performance, with excellent thermal and chemical stability [1–3]. Of phosphate-based materials, the $LiMPO_4(OH)$ (M = Mn, Fe) system with a tavorite-like structure [4,5] appears to be a promising cathode material because (i) it has a theoretical capacity of ca. 160 mAh g^{-1} for one-electron reaction; (ii) Mn and Fe are safe and inexpensive transition metals and a high redox potential is expected due to M^{3+} ions in the compound; and (iii) its three-dimensional framework consists of MO_6 octahedral chains bridged by PO_4 tetrahedra and thus provides two possible lithium sites in diffusion tunnels and hydroxy groups OH^-, which produce a bottleneck in the lithium diffusion path, may enhance lithium ion hopping due to the reduced interaction between Li^+ and O^{2-} ions. Consequently, investigating this material may enable the realization of high-performance electrodes for lithium batteries.

Lithium iron hydroxyphosphate with the tavorite structure, $LiFePO_4(OH)$, exhibits a capacity of about 100 mAh g^{-1} with an average voltage of ~2.3 V (vs. Li^+/Li) in the voltage range of 2.0–4.6 V [5]. However, its electrochemical activity is attributed to a Fe^{3+}/Fe^{2+} redox reaction during discharge because extraction of Li^+ from the lattice was not observed during initial charging process due to the high redox potential of Fe^{3+}/Fe^{4+}, which exceeded the voltages used in the measurement. On the other hand, isostructural $LiMnPO_4(OH)$ exhibits a higher electrochemical activity (110 mAh g^{-1}) and a higher average voltage (3.4 V vs. Li^+/Li) than $LiFePO_4(OH)$, but a phase transition occurs in the initial charge–discharge process in the voltage range of 2.0–4.6 V [6]. The key properties of this important class of materials are the structural characteristics including a Jahn–Teller ion Mn^{3+} in the crystal lattice, which influences the electrode performance of the Mn^{3+} phase [7]. A $LiMn_{1-x}Fe_xPO_4(OH)$ solid-solution system may be able to provide continuous information about the crystal structure and electrochemical characteristics as a function of composition.

In the present study, the $LiMn_{1-x}Fe_xPO_4(OH)$ solid solution was synthesized by a H^+/Li^+ exchange reaction using $LiNO_3$ and $Mn_{1-x}Fe_xPO_4{\cdot}H_2O$. The detailed structures of the $LiMn_{1-x}Fe_xPO_4(OH)$ solid solution were systematically investigated by synchrotron-radiation (SR) X-ray diffraction (XRD) and Rietveld refinement. The electrode performances were

* Corresponding author. Tel.: +81 459245401; fax: +81 459245401.
E-mail addresses: yang@echem.titech.ac.jp (Y. Yang), hirayama@echem.titech.ac.jp (M. Hirayama), kubota@echem.titech.ac.jp (K. Kubota), kanno@echem.titech.ac.jp (R. Kanno).

0378-7753/$ – see front matter © 2012 Elsevier B.V. All rights reserved.
doi:10.1016/j.jpowsour.2011.12.041

characterized by charge–discharge measurements. The effect of iron substitution is discussed.

2. Experimental

The precursor $Mn_{1-x}Fe_xPO_4{\cdot}H_2O$ was prepared by a hydrothermal method [8]. Saturated solutions of $Mn(NO_3)_2{\cdot}6H_2O$ (Wako, Ltd.; >98 wt.%) and Fe $(NO_3)_3{\cdot}9H_2O$ (Wako, Ltd.; >99.8 wt.%) were mixed with Mn/Fe molar ratios of 1/0, 9/1, 8/2, 7/3, 5/5, 3/7, 1/9, and 0/1 and then added to an excess acid solution (1.85 M) H_3PO_4 (Wako, Ltd.; >85 wt.%) under magnetic stirring. The final solution was transferred to an autoclave and heated at 160 °C for 2–4 h. The resulting powders were washed with distilled water and then dried for 12 h at 60 °C under vacuum. The obtained $Mn_{1-x}Fe_xPO_4{\cdot}H_2O$ was mixed with $LiNO_3$ (Wako, Ltd.; >98 wt.%) with a molar ratio of 1:4 by ball milling for 2 h. The mixture was heated at 200 °C in air, washed with distilled water, and dried in vacuum at 60 °C. Brownish powders were then obtained.

XRD patterns were obtained at room temperature using a Rigaku SmartLab diffractometer with Cu Kα radiation in the 2θ range of 10–70° with a step scan interval of 0.02° for a counting time of 3 s. Inductively coupled plasma (ICP) atomic emission spectrometry analysis was used to perform elemental analysis of Li, Mn, Fe, and P using a Prodigy ICP atomic emission spectrometer. Spectra were obtained after the $LiMn_{1-x}Fe_xPO_4(OH)$ powder had been completely dissolved in hydrochloric acid solution. The morphologies of powder samples were investigated by high-resolution scanning electron microscopy (SEM) using a Hitachi S-4700 microscope. Carbon coating was performed to reduce charging of samples during SEM observations. Their thermal stabilities were investigated by performing thermogravimetry–differential thermal analysis (TG–DTA) with a Rigaku Instrument Thermo plus TG 8120 at a heating rate of 5 °C min^{-1} in an argon atmosphere.

The crystal structure of $LiMn_{1-x}Fe_xPO_4(OH)$ was investigated by SR-XRD measurements at the SPring-8 facility on a Debye–Scherrer diffractometer installed in beam line BL02B2 [9]. Samples were sealed in Lindemann capillaries (ca. 0.3 mm) under an argon atmosphere prior to measurement. Diffraction patterns were obtained with a wavelength of 0.59866 Å at room temperature in the angular range of 3.0–70.0° with a 0.01° (2θ) step. The incident beam wavelength was calibrated using a NIST SRM Ceria 640b CeO_2 standard. The SR-XRD data were analyzed by Rietveld refinement using the structural model $Li_{2i}\{(Mn1)_{1a}(Mn2)_{1b}\}(P)_{2i}(O)_{2i}H_{2i}$ (space group: P–1) [10] and the program Rietan-FP [11]. The split pseudo-Voigt function proposed by Toraya [12] was used in the refinements of the SR-XRD data.

The electrochemical performances of $LiMn_{1-x}Fe_xPO_4(OH)$ were investigated by performing charge–discharge measurements using 2032 coin cells assembled in an argon-filled glove box. The cells were aged for 24 h at room temperature before the charge–discharge tests. The negative electrode was a disk of lithium metal foil. A polypropylene separator (Celgard) that had been soaked in a solution of 1 mol l^{-1} $LiPF_6$ in ethylene carbonate/diethyl carbonate (3:7 vol.%) was placed between the two electrodes. A positive electrode was fabricated by mixing 80 wt.% of the active material $LiMn_{1-x}Fe_xPO_4(OH)$ and 15 wt.% of Ketjen Black (ECP, Akzo Nobel) with 5 wt.% polyvinylidene fluoride in N-methylpyrrolidone. Strong mixing between the active material and the carbon powder was achieved by ball milling the mixture for 60 min at 240 rpm using a Fritsch ball mill. The obtained slurry was spread onto an aluminum foil using a doctor blade and a disk electrode was obtained after drying at 120 °C in a vacuum for 6 h. The charge–discharge characteristics were measured at room temperature over the voltage range of 2.0–4.6 V vs. Li^+/Li at a constant rate of 1/100 C (which corresponds to the theoretical exchange for one electron per formula during charging or discharging for 100 h).

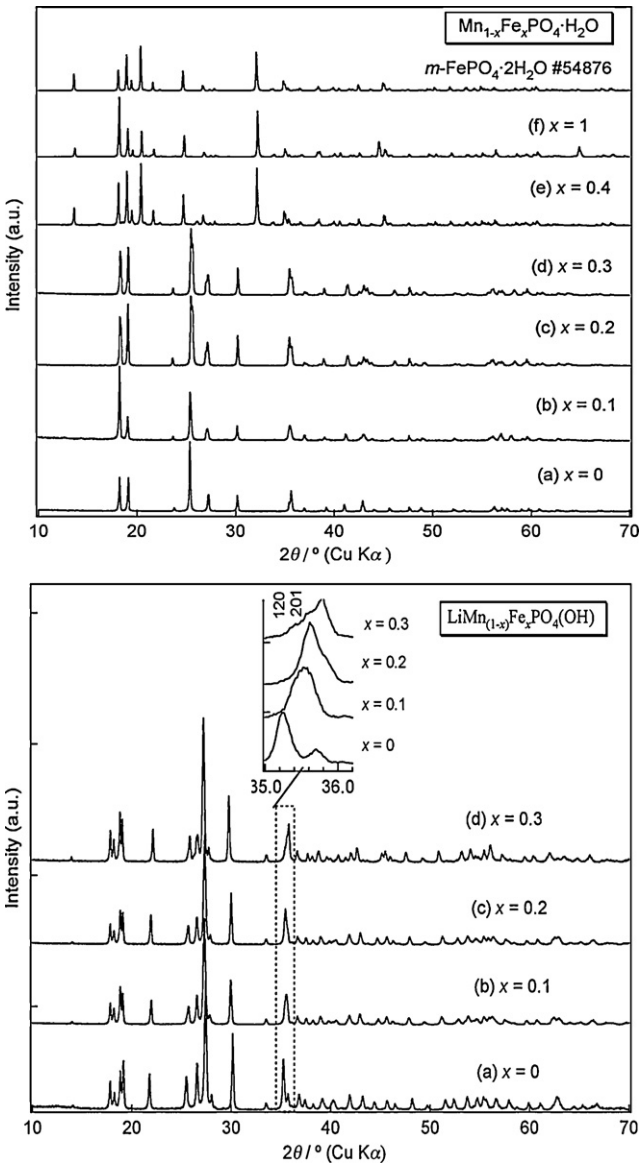

Fig. 1. XRD patterns of $Mn_{1-x}Fe_xPO_4{\cdot}H_2O$ and $LiMn_{1-x}Fe_xPO_4(OH)$.

3. Results and discussion

Fig. 1 shows XRD patterns of the hydrate precursors $Mn_{1-x}Fe_xPO_4{\cdot}H_2O$ ($0 \le x \le 1$) and the products of the ion-exchange reaction. For the $Mn_{1-x}Fe_xPO_4{\cdot}H_2O$ series, XRD patterns of the compounds in the composition range x = 0.0–0.3 could be indexed to the lattice of $MnPO_4{\cdot}H_2O$ with space group $C2/c$ except that the diffraction angles are shifted to higher 2θ values, which indicates a smaller lattice. This smaller lattice can be attributed to the ionic radius of Fe^{3+} (0.55 Å) being smaller than that (0.58 Å) of Mn^{3+} ions [13]. For iron contents (x) in the range 0–0.4, multiphase powders with m-$FePO_4{\cdot}2H_2O$ as the main impurity phase were obtained [14]. These results suggest that the solid solution $Mn_{1-x}Fe_xPO_4{\cdot}H_2O$ has a small miscibility gap under the hydrothermal reaction conditions. All the diffraction peaks of the ion-exchanged phases $LiMn_{1-x}Fe_xPO_4(OH)$ ($0 \le x \le 0.3$) could be indexed to the structure of $LiMnPO_4(OH)$ with space group P–1 [10]. Furthermore, the profiles vary as a function of the Fe^{3+} content, as shown in Fig. 1 for the (−1 0 2), (1 0 1), (1 2 0),

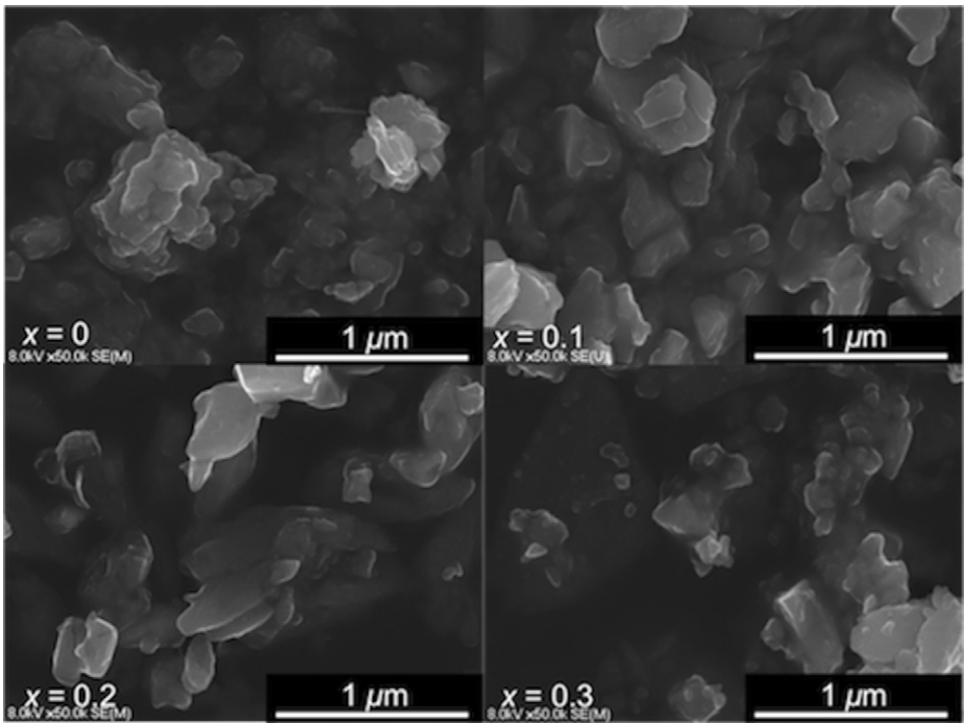

Fig. 2. SEM images of $LiMn_{1-x}Fe_xPO_4(OH)$ samples for $x = 0$, 0.1, 0.2 and 0.3.

and (2 0 1) diffraction peaks of the $LiMn_{1-x}Fe_xPO_4(OH)$; this indicates that decreasing Mn^{3+} concentration induces an anisotropic change in the orthorhombicity. As mentioned above, the XRD data for all the samples imply that solid solutions $LiMn_{1-x}Fe_xPO_4(OH)$ with the tavorite structure are obtained for Fe substitution up to $x = 0.3$. In the present study, only single-phase $LiMn_{1-x}Fe_xPO_4(OH)$ ($0 \le x \le 0.3$) are characterized.

The chemical compositions of the above phases were clarified by ICP elemental analysis. Table 1 compares the estimated compositions of the samples with the target compositions. The Mn to Fe

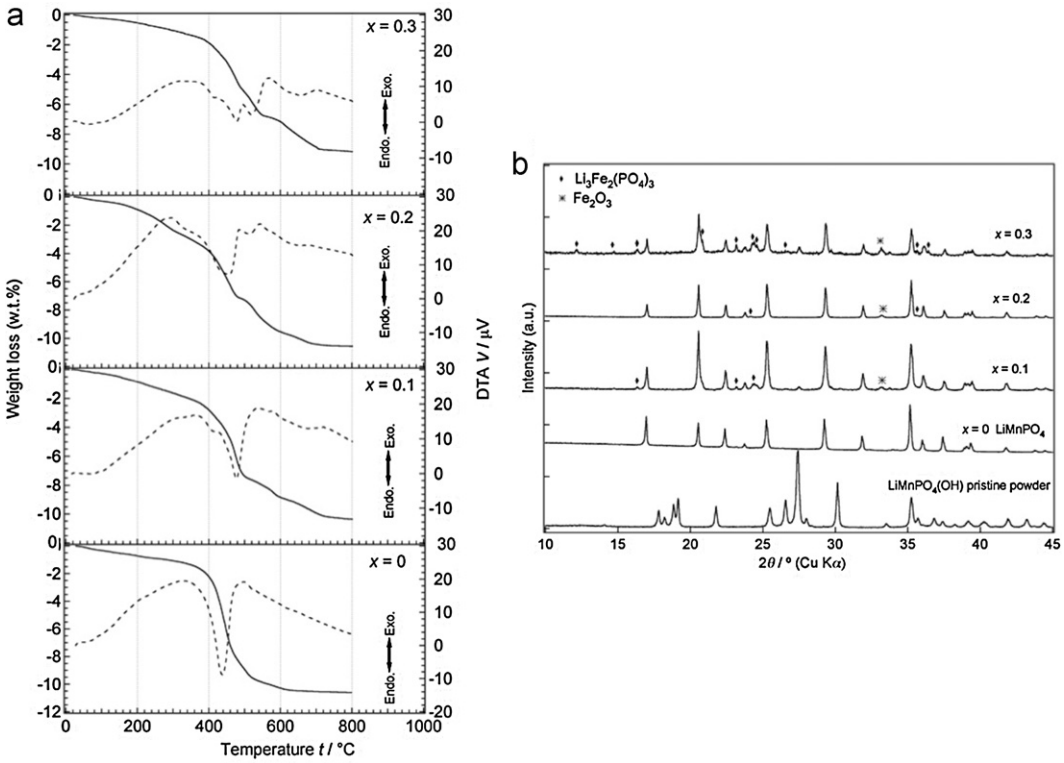

Fig. 3. (a) TG curve (solid line) and DTA curve (dotted line) for $LiMn_{1-x}Fe_xPO_4(OH)$ measured between 25 and 800 °C at a rate of 5 °C min^{-1} in an argon atmosphere. (b) XRD patterns of $LiMn_{1-x}Fe_xPO_4(OH)$ decomposition products after TG–DTA measurements.

Table 1
Intended and observed compositions of $LiMn_{1-x}Fe_xPO_4(OH)$.

Intended composition	Observed composition
$LiMnPO_4(OH)$	$LiMnPO_4(OH)$
$LiMn_{0.9}Fe_{0.1}PO_4(OH)$	$Li_{0.8797}Mn_{0.8941}Fe_{0.0972}PO_4(OH)$
$LiMn_{0.8}Fe_{0.2}PO_4(OH)$	$Li_{0.8913}Mn_{0.8207}Fe_{0.1815}PO_4(OH)$
$LiMn_{0.7}Fe_{0.3}PO_4(OH)$	$Li_{0.9125}Mn_{0.6812}Fe_{0.3205}PO_4(OH)$

concentration ratios are generally close to those of the expected compositions. Furthermore, nearly half the protons in the monohydrate precursor $Mn_{1-x}Fe_xPO_4{\cdot}H_2O$ were exchanged by lithium ions, which indicates that H^+/Li^+ ion exchange is close to completion. Fig. 2 shows typical SEM images of $LiMn_{1-x}Fe_xPO_4(OH)$ series samples. The SEM images reveal irregular, agglomerated particles with sizes of the order of hundreds of nanometers; these particles were observed for all iron contents examined in the present study.

The structural stability of $LiMn_{1-x}Fe_xPO_4(OH)$ with $x = 0$, 0.1, 0.2, and 0.3 was investigated by heating the materials in argon in the temperature range 25 and 800 °C; the results are displayed in Fig. 3a. The main weight loss attributed to dehydration is observed between 350 and 500 °C. For the Mn-only phase ($x = 0$), only one endothermic peak is observed at about 420 °C. In contrast, shoulders appear on the low and high temperature sides of this DTA peak for samples with $x \geq 0.1$. The shoulder on the high temperature side becomes more prominent with increasing x and evolves into a major peak in the sample with $x = 0.3$. The decomposition temperatures of the samples (taken to be the onset of the main peak) increase from 430 to 470 °C as the iron content increases from 0 to 30%. Fig. 3b shows XRD patterns of the final decomposition products obtained after TG–DTA measurements. The samples heated to 800 °C could be completely indexed as a mixture of $LMnPO_4$, $Li_3Fe_2(PO_4)_3$, and Fe_2O_3, in agreement with the following reactions:

$$LiMnPO_4(OH) \rightarrow LiMnPO_4 + (1/2)H_2O + (1/4)O_2 \quad (1)$$

$$LiFePO_4(OH) \rightarrow (1/3)Li_3Fe_2(PO_4)_3 + (1/6)Fe_2O_3 + (1/2)H_2O \quad (2)$$

The weight losses determined from TGA plots were −10.1, −10.5, −10.3, and −9.2% for $LiMn_{1-x}Fe_xPO_4(OH)$ ($x = 0$, 0.1, 0.2, and 0.3), which approximately correspond to the calculated values based on the decomposition reactions (1) and (2), namely −9.8, −9.5, −9.0, and −9.2% for $x = 0$, 0.1, 0.2, and 0.3, respectively. The thermal stability results suggest that the decomposition temperature of the solid solution increases with increasing iron content.

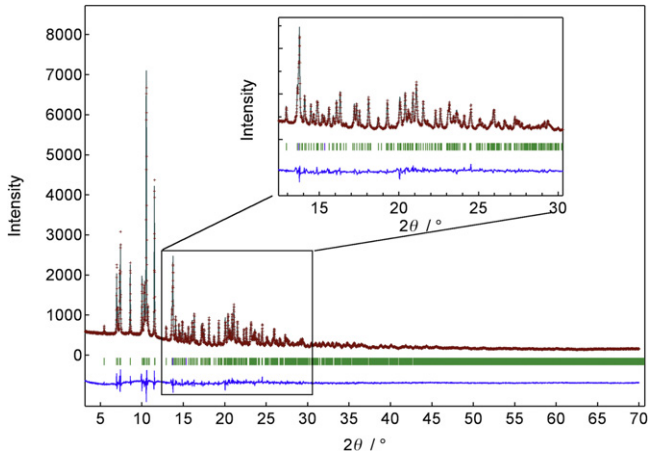

Fig. 4. Observed (plus signs), calculated (solid line), and difference (bottom) profiles for the Rietveld refinement from synchrotron X-ray data of $LiMn_{1-x}Fe_xPO_4(OH)$. The short vertical lines below the profiles indicate the peak positions of all possible Bragg reflections.

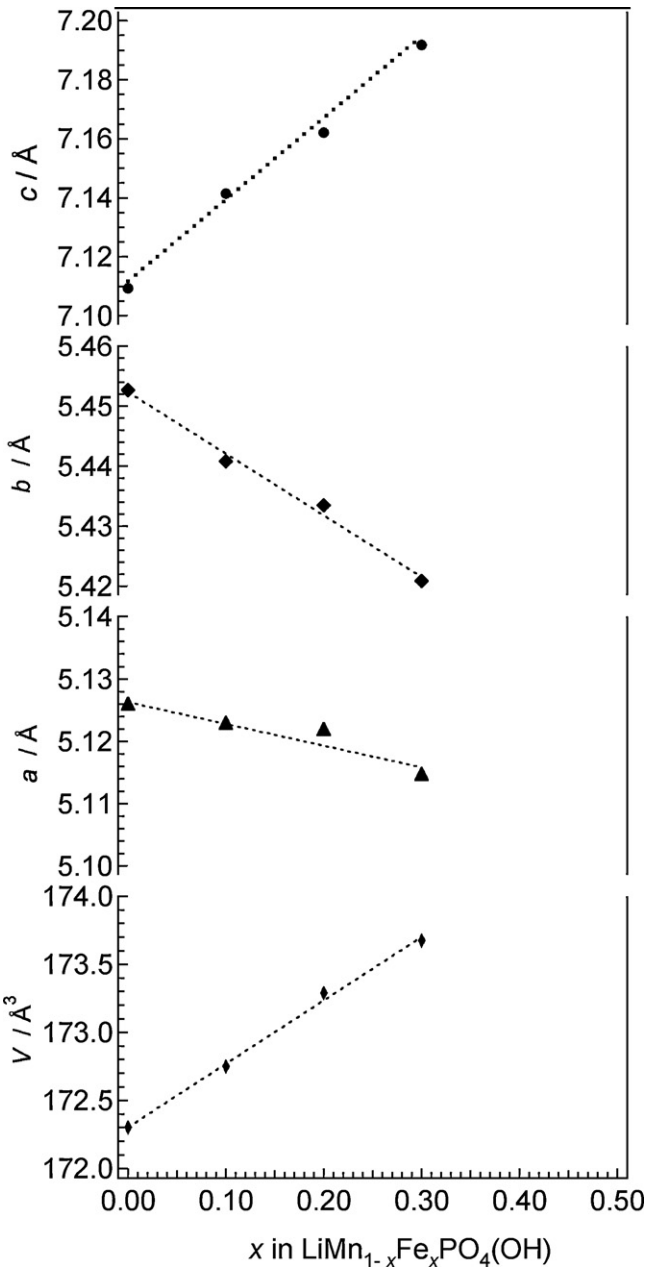

Fig. 5. Lattice parameters of $LiMn_{1-x}Fe_xPO_4(OH)$ as a function of iron content.

To further evaluate the change to the crystal geometry caused by iron substitution, the structure of each $LiMn_{1-x}Fe_xPO_4(OH)$ ($0 \leq x \leq 0.3$) solid solution was carefully refined against the synchrotron powder XRD patterns. The SR-XRD data of $LiMn_{1-x}Fe_xPO_4(OH)$ were refined to the compositions containing no impurity phases using a crystal structure model of $LiMPO_4(OH)$ with space group P–1 as follows [10]: Li in 2*i* (0.24, 0.618, 0.23); *M*1 in 1*a* (0, 0, 0); *M*2 in 1*b* (0, 0, 0.5); P in 2*i* (−0.324, 0.371, 0.235); O1 in 2*i* (0.1106, 0.6462, −0.121); O2 in 2*i* (−0.6945, −0.2375, 0.6004); O3 in 2*i* (0.3028, 0.3406, −0.337); O4 in 2*i* (−0.3671, −0.2479, 0.9442); O5 in 2*i* (0.1656, −0.0306, 0.2813); H in 2*i* (0.3744, 0.0738, 0.3454). The hydrogen atom was fixed at the initial position 2*i* and lithium deficiency was considered during the refinement. The compound $LiMn_{0.7}Fe_{0.3}PO_4(OH)$ showed the best agreement between the calculated and the observed profiles; it was representative of all the compounds (see Fig. 4). Rietveld refinement indicated reliable indices of $R_{wp} = 5.64\%$ and

Table 2
Structural parameters of $LiMn_{0.7}Fe_{0.3}PO_4(OH)$ determined by synchrotron Rietveld refinement analysis at 27 °C.

Atom	Site	g	x	y	z	B (Å^2)
Li(1)	2*i*	0.91(3)	0.286(5)	0.629(4)	0.200	2.8(2)
Mn(1)	1*a*	=0.7	0	0	0	0.36(4)
Mn(2)	1*b*	=0.7	0	0	1/2	0.59(1)
Fe(1)	1*a*	0.3	0	0	0	=Mn(1)
Fe(2)	1*b*	0.3	0	0	1/2	=Mn(2)
P(1)	2*i*	1.0	−0.328(3)	0.369(2)	0.237(2)	0.61(5)
O(1)	2*i*	1.0	0.109(2)	0.648(4)	0.875(3)	0.57(3)
O(2)	2*i*	1.0	0.272(3)	0.771(4)	0.607(2)	=O(1)
O(3)	2*i*	1.0	0.319(2)	0.328(4)	0.667(4)	=O(1)
O(4)	2*i*	1.0	0.637(3)	0.747(2)	0.918(2)	=O(1)
O(5)	2*i*	1.0	0.141(7)	−0.048(3)	0.275(3)	=O(1)
H	2*i*	1.0	0.376	0.085	0.352	1.0

Unit cell: *P*–1(2); $a = 5.1149(3)$ Å, $b = 5.4218(7)$ Å, $c = 7.1926(5)$ Å, $\alpha = 106.946(3)^\circ$, $\beta = 108.204(2)^\circ$, $\gamma = 99.658(5)^\circ$, $V = 173.75(3)$ Å^3; $R_{wp} = 5.64$, $R_p = 4.45$, $R_e = 5.58$, goodness of fit $S = R_{wp}/R_e = 1.01$, $R_B = 5.57$, $R_F = 1.83$.

Table 3
Structure parameters of the $LiMn_{1-x}Fe_xPO_4(OH)$ compositions with $x = 0$, 0.1, 0.2, and 0.3.

$LiMn_{1-x}Fe_xPO_4$ (OH)	a (Å)	b (Å)	c (Å)	α (°)	β (°)	γ (°)	V (Å^3)	R_{wp} (%)
$x = 0$	5.1257(9)	5.4527(10)	7.1094(15)	106.251(14)	108.159(12)	101.300(12)	172.3(2)	2.23
$x = 0.1$	5.1225(7)	5.4407(5)	7.1612(9)	106.751(12)	108.172(12)	100.438(5)	173.47(6)	5.8
$x = 0.2$	5.1216(5)	5.4335(8)	7.1621(8)	106.791(11)	108.185(10)	100.275(8)	173.59(2)	5.3
$x = 0.3$	5.1149(3)	5.4218(7)	7.1926(5)	106.946(3)	108.204(2)	99.658(5)	173.75(3)	5.6

Table 4
Interatomic distances (Å) in structural polyhedra. The distortion is calculated using $\Delta_d = (1/N)\sum_{n-1}^{N}((d_n - \langle d\rangle)/\langle d\rangle)^2$, where d_n is the bond length n, $\langle d\rangle$ is the average bond length, and N is the number of bonds.

	$x = 0$	$x = 0.1$	$x = 0.2$	$x = 0.3$
*M*1—O1 × 2	2.160(3)	2.146(2)	2.123(4)	2.093(2)
*M*1—O4 × 2	1.892(1)	1.909(2)	1.925(1)	1.939(2)
*M*1—O5 × 2	1.988(2)	1.985(1)	1.982(1)	1.983(2)
Mean	2.013	2.014	2.011	2.004
Δ_d	3.0×10^{-3}	2.4×10^{-3}	1.8×10^{-3}	1.1×10^{-3}
*M*2—O2 × 2	2.192(2)	2.178(3)	2.152(2)	2.129(1)
M2—O3 × 2	1.898(3)	1.915(2)	1.937(1)	1.963(2)
*M*2—O5 × 2	1.930(1)	1.933(3)	1.935(2)	1.941(1)
Mean	2.007	2.009	2.008	2.011
Δ_d	4.3×10^{-3}	3.6×10^{-3}	2.6×10^{-3}	1.7×10^{-3}
P—O1	1.558(3)	1.567(2)	1.576(1)	1.581(2)
P—O2	1.516(3)	1.524(2)	1.531(1)	1.537(4)
P—O3	1.507(1)	1.516(2)	1.525(2)	1.535(3)
P—O4	1.510(2)	1.507(2)	1.503(2)	1.497(3)
Mean	1.523	1.529	1.534	1.538
Δ_d	1.9×10^{-4}	2.1×10^{-4}	2.9×10^{-4}	3.9×10^{-4}
Li—O1(1)	1.956(3)	1.985(2)	2.038(1)	2.107(1)
Li—O1(2)	2.223(2)	2.229(1)	2.245(3)	2.256(3)
Li—O2	2.741(3)	2.777(2)	2.813(1)	2.845(1)
Li—O3	2.161(3)	2.112(1)	2.084(3)	2.041(2)
Li—O4	2.256(3)	2.257(3)	2.251(2)	2.245(1)
Li—O5	1.964(1)	1.945(1)	1.937(2)	1.908(2)
Mean	2.217	2.218	2.228	2.234
Δ_d	1.4×10^{-2}	1.5×10^{-2}	1.6×10^{-2}	1.8×10^{-2}

$S = R_{wp}/R_e = 1.1$ (see Table 2), which are sufficiently reasonable to discuss the local crystal geometry (see below). The octahedral coordinated cations in the tavorite $LiMn_{1-x}Fe_xPO_4(OH)$ series are completely ordered between the lithium and *M*1 and *M*2 sites. Li occupies only the 2*i* site, whereas trivalent Mn and Fe ions occupy various kinds of the two *M*1 and *M*2 sites. The refinement results are summarized in Table 3 for the series of $LiMn_{1-x}Fe_xPO_4(OH)$ compositions with $x = 0$, 0.1, 0.2, and 0.3 and the composition dependence of the lattice parameters is shown in Fig. 5. It shows a linear decrease in the unit cell dimensions a and b and a linear increase in the cell parameter c and the cell volume with increasing Fe content, which indicates the formation of continuous solid solution $LiMn_{1-x}Fe_xPO_4(OH)$. The results suggest that the substitution of Fe^{3+} for Mn^{3+} should give rise to a different local geometry due to a change in the polyhedron bond length.

Table 4 summarizes the bond lengths in MO_6, LiO_6, and PO_4 polyhedra obtained by refinement. Fig. 6 shows the crystal structure of $LiMPO_4(OH)$ and the local geometry of MO_6 and PO_4 polyhedral. It is clearly apparent that Li and H atoms reside in the tunnels along the a axis. Lithium ions may migrate along the zigzag line in the [1 0 0] direction through a bottleneck formed by the O1(1), O1(2), O4, and O5 sites (red tetrahedron). We consider the extent to which the local structural changes in the polyhedra vary with iron substitution. The variations of the bond lengths *M*—O in MO_6, Li—O in LiO_6 octahedra, and P—O in PO_4 tetrahedra are depicted in Fig. 7 for series $LiMn_{0.7}Fe_{0.3}PO_4(OH)$ ($0 \le x \le 0.3$) compounds. The small

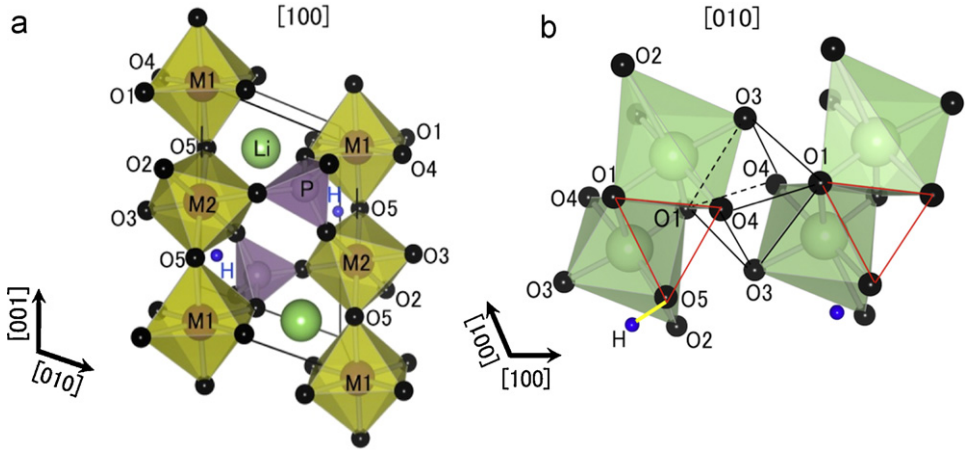

Fig. 6. Local geometry of the polyhedra in LiMPO_4(OH) crystal structure: (a) MO_6 octahedra along [0 0 1] direction and (b) LiO_6 octahedral along [1 0 0] direction.

rigid PO_4 tetrahedron in all series of samples shows a slight distortion ($\Delta_d = 1.9–3.9 \times 10^{-4}$) with P—O distances in the range of 1.50–1.58 Å, which could be attributed to the strong covalent P—O bond. The transition metal cations Mn and Fe lie in the octahedral site *M*1 and *M*2 shares corners through two O5 atoms with the neighboring MO_6, which share corners through O1 and O4 with *M*1 and through O2 and O3 atoms with *M*2 with four PO_4 tetrahedra. The MO_6 octahedra show large distortions with *M*—O distances in the range of 1.89–2.16 Å for *M*1 and 1.90–2.19 Å for *M*2. The $M^{3+}O_6$ octahedra relax slightly with a reduction in the concentration of Jahn–Teller active Mn^{3+} ions with strong selective elongation of the two equatorial (*a* direction) bond lengths *M*1—O4 and *M*2—O3 and shrinkage of the two axial (*c* direction) bond lengths *M*1—O1 and *M*2—O2. An equatorial/axial ratio of *c*/*a*, which indicates the degree of Jahn–Teller distortion, decreases from 1.14 to 1.08 for $M1O_6$ and from 1.15 to 1.08 for $M2O_6$. However, equatorial elongation was observed only for *M*1—O4 and *M*2—O3, whereas the other two equatorial bond lengths *M*1—O5 and *M*2—O5 change very little. The corner-sharing geometry of $M^{3+}O_6$ and the strong interaction between O5—H···O2 may fix the shared O5 and give rise to strong selective elongation of the *M*1—O4 and *M*2—O3 distances in the 2O4—*M*1—2O5 and 2O3—*M*2—2O5 equatorial planes, respectively. Furthermore, the bond-length variations at the Li sites suggest that LiO_6 is affected by interactions with neighboring polyhedra. The Li—O1(1), Li—O1(2), and Li—O2 bond lengths increase, whereas the Li—O3, Li—O4, and Li—O5 bond lengths decrease with increasing Fe

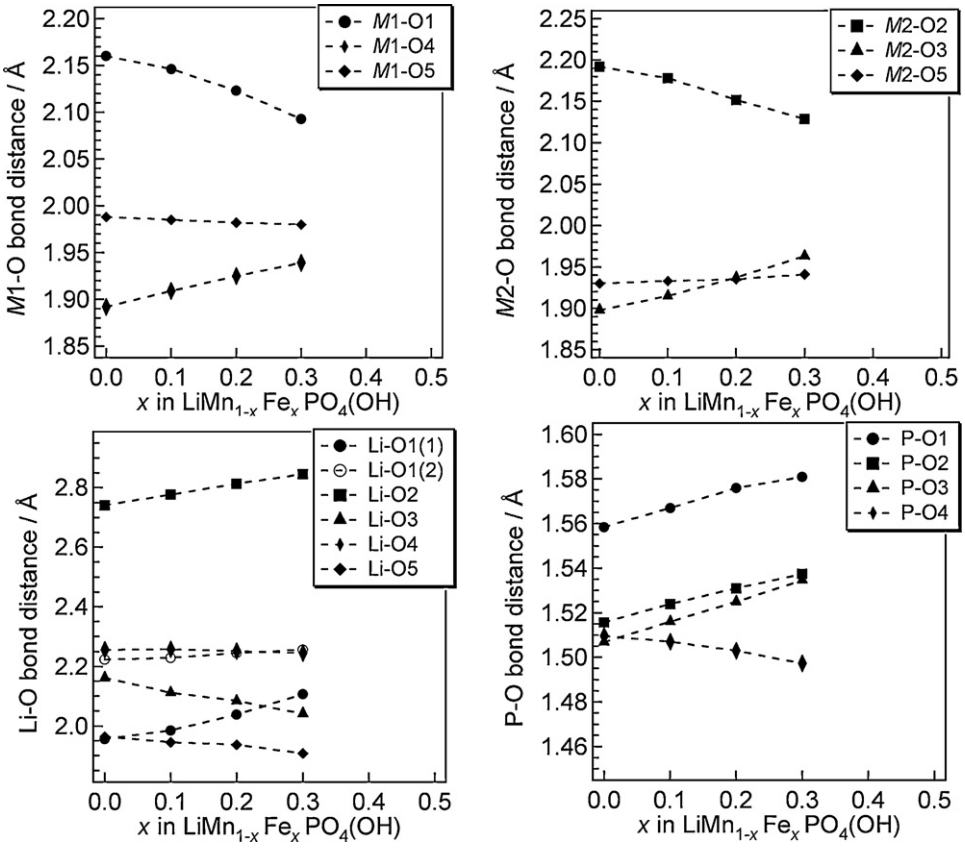

Fig. 7. Interatomic distances for (a) *M*1—O, (b) *M*2—O, (c) Li—O, and (d) P—O as a function of $LiMn_{1-x}Fe_xPO_4$(OH) composition.

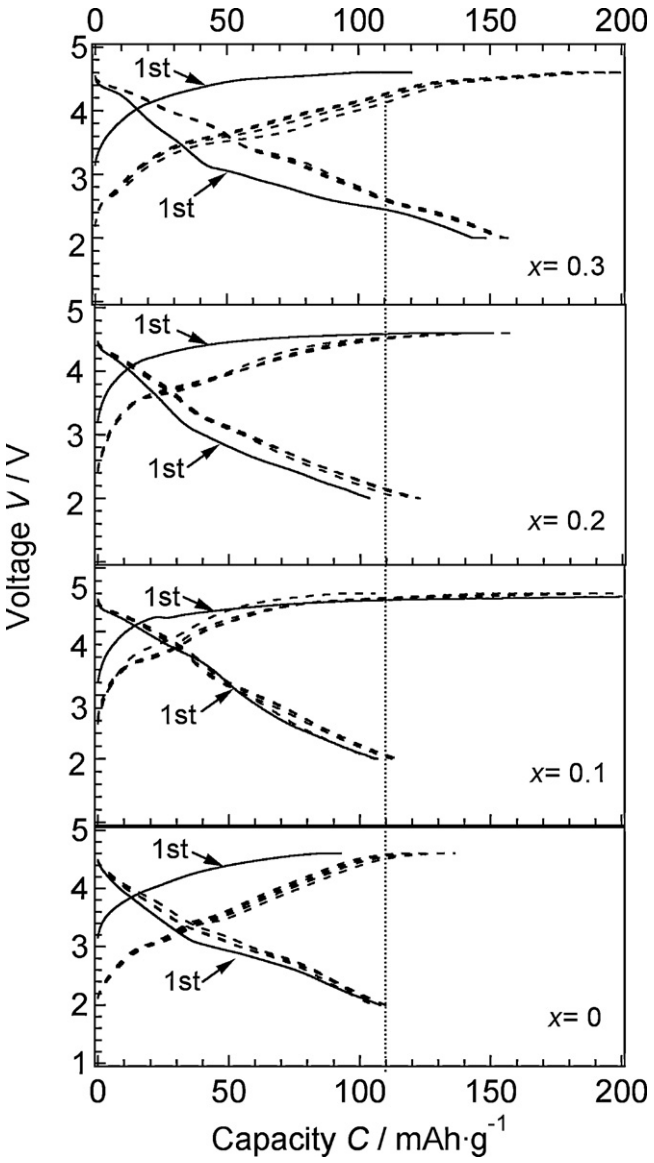

Fig. 8. Charge–discharge curves for the Li/$LiMn_{1-x}Fe_xPO_4(OH)$ cell up to 10 cycles measured at 25 °C at a rate of C/100.

substitution. The average Li—O bond length increases from 2.217 to 2.234 Å as the iron content x increases from 0 to 0.3. The much larger elongation of Li—O1(1) and Li—O1(2) than the shrinkage of Li—O4 and Li—O5 indicates a weaker Coulomb attractive force between the Li^+ and surrounding O^{2-} ions in the bottleneck, which may facilitate lithium ion diffusion in the crystal lattice. Hence, we focused on the electrode performance of $LiMn_{0.7}Fe_{0.3}PO_4(OH)$, which should be influenced by the local structural changes, such as the enhanced asymmetry in MO_6 and the facilitated diffusion path for lithium ions.

Fig. 8 shows the charge–discharge curves measured for the $LiMn_{1-x}Fe_xPO_4(OH)$ series with $x = 0$, 0.1, 0.2, and 0.3 at a rate of C/100. During the initial charge, the solid solution phases have similar profiles to that of the end phase $LiMnPO_4(OH)$. The voltage increases rapidly to about 3.8 V and it then increases gradually to the cut-off voltage of 4.6 V. The charge capacity increases gradually from 80 mAh g^{-1} (ca. 0.5 lithium per unit) to 100 mAh g^{-1} (ca. 0.64 lithium per unit) as the Fe content x increases from 0 to 0.3. In contrast, the initial discharge curves show a slow increase and a voltage plateau at ~3 V. The discharge capacity increases gradually and the plateaus become increasingly pronounced with increasing Fe content. The discharge capacity increases from 110 mAh g^{-1} for $LiMnPO_4(OH)$ to 150 mAh g^{-1} for $LiMn_{0.7}Fe_{0.3}PO_4(OH)$ when the $LiMn_{1-x}Fe_xPO_4(OH)$/Li cells are discharged to 2.0 V. In the following cycles, two charge–discharge plateaus appear at ~3.5 and ~2.5 V respectively and they become increasingly pronounced with increasing Fe content. As the decreasing polarization in the 3.5 V plateau, the electrochemical activity of Mn^{4+}/Mn^{3+} increases with increasing iron content. Therefore, the electrochemical activity of Mn^{4+}/Mn^{3+} in $LiMn_{1-x}Fe_xPO_4(OH)$ is not solely determined by the inherent activity of Mn^{4+}/Mn^{3+} in $LiMn_{1-x}Fe_xPO_4(OH)$; it is also dependent on the amount of Fe^{3+} ions coexisting in octahedral sites. Furthermore, the Columbic efficiency of the charge-discharge is lower in the subsequent cycles than that in the initial cycle, which is probably due to the irreversible decomposition of electrolyte at the 4.6 V plateau. It indicates that the redox reactions of $Mn^{3+/2+}$ and $Fe^{3+/2+}$ may occur during charging in the first cycle and compensate the charge capacity caused by electrolyte decomposition, corresponding to the larger discharge capacity in the initial cycle. The above results suggest that the electrode performance of $LiMnPO_4(OH)$ can be improved by partial substitution of manganese by iron.

To understand the electrochemical reactions during the charge–discharge process, dQ/dV data were obtained from the charge–discharge curves. Fig. 9 shows differential plots (dQ/dV) in the first, second, and fifth cycles of the charge–discharge curves for the Li/Li^+/$LiMn_{1-x}Fe_xPO_4(OH)$ cell. For the initial cycle, weak anodic peaks A1a at a voltage near 4.0 V are observed for all series and the peaks shift to higher voltages as the Fe content x increases from 0 to 0.3. Two cathodic peaks C1a and C1e appear during discharge at voltages at around 4.0 and 4.3 V respectively. When the cell is discharged to 2.0 V, two cathodic peaks C1b and C1c were observed at 2.9 and 2.6 V respectively and they shifted to lower voltages with increasing Fe content. Furthermore, a noticeable cathodic peak for the iron-substituted phase $LiMn_{1-x}Fe_xPO_4(OH)$ ($x \neq 0$) appeared at 2.5 V and it shifted to a lower voltage with increasing iron content. This is consistent with the sloping discharge curve and the very short plateau at about 2.5 V for the solid solution samples, especially at $x = 0.3$. The redox peak intensities at this voltage for $LiMn_{1-x}Fe_xPO_4(OH)$ increase gradually with increasing iron content, which corresponds to the increased capacity in the region of 2 V observed in the charge–discharge performance.

In the second cycle, anodic peaks appear around 2.5 V implying reversible (de)intercalation of lithium ions in $LiMn_{1-x}Fe_xPO_4(OH)$ at this voltage during the charge–discharge process. Furthermore, two pairs of strong redox peaks A2b and C2b at a voltage of about 3.3 V and A2c and C2c at about 2.9 V develop, which indicate that several reaction steps occur between 2.0 and 4.0 V. The oxidation peaks Aa from the 2nd cycle are lower than that in the 1st charge and the redox couples Ad/Cd, Ac/Cc, and Ab/Cb are reversible after the 2nd cycle. This indicates that reverse redox reactions of $Mn^{3+/2+}$ and $Fe^{3+/2+}$ occur in the subsequent cycles. All these redox peaks are relatively broad, indicating a solid-solution lithiation/delithiation mechanism for $LiMn_{1-x}Fe_xPO_4(OH)$. In addition, the difference between the oxidation and reduction peaks suggests a large polarization in $LiMn_{1-x}Fe_xPO_4(OH)$ samples, corresponding to the large overvoltage in the charge–discharge curves. The peak intensities gradually decrease with cycling, which is in good agreement with the observed deterioration in the capacity after the second cycle.

The appearance of the reversible redox pairs Ac/Cc and Ab/Cb at around 2.9 and 3.3 V respectively, indicates that a phase change also occurred in $LiMn_{1-x}Fe_xPO_4(OH)$ during the charge–discharge process. The irreversible phase change during the first charge–discharge process causes a phase with higher capacity where the intercalation proceeds reversibly by two-step phase changes. On the other hand, the improved charge–discharge

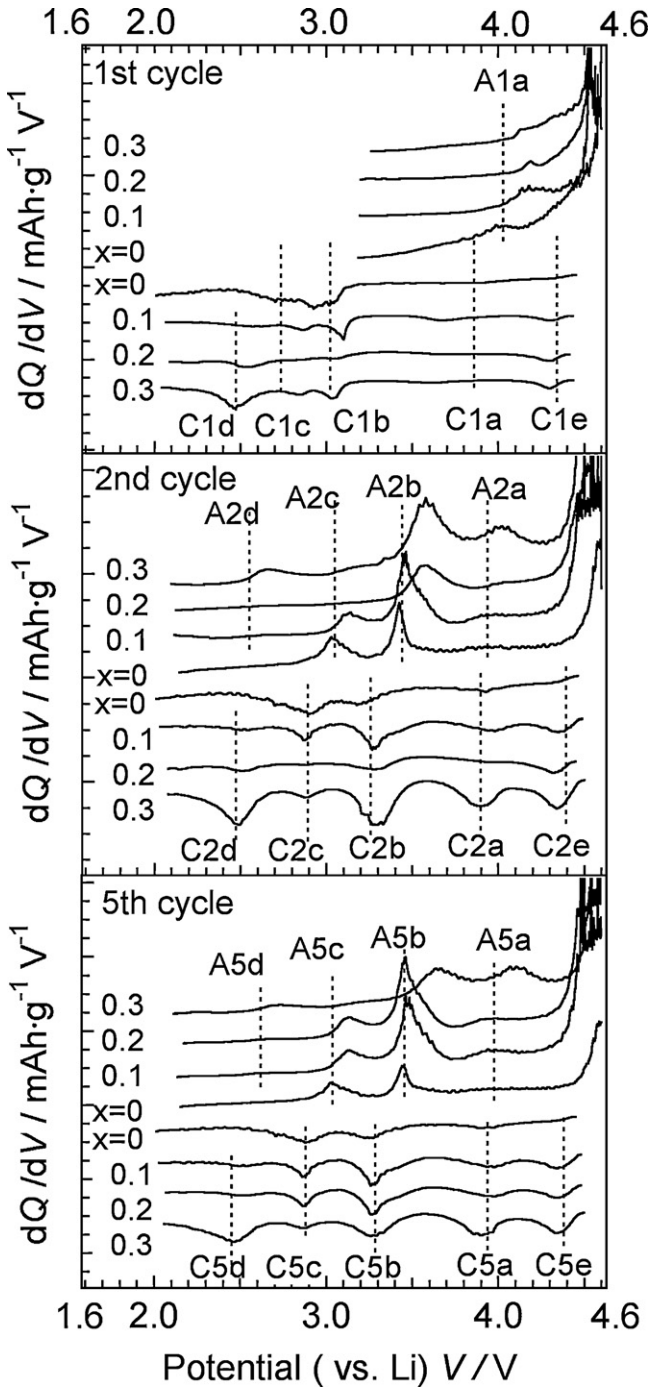

Fig. 9. Differential capacity curves for cycling of $LiMn_{1-x}Fe_xPO_4(OH)$ ($x = 0$, 0.1, 0.2, and 0.3) obtained between 2.0 and 4.6 V (vs. Li^+/Li) at a rate of C/100 for the (1) initial, (2) second, and (3) fifth cycles.

performance on iron substitution suggests that the local geometry change in the crystal structure caused by Fe^{3+} substitution at Mn^{3+} sites could affect the electrode performance of $LiMnPO_4(OH)$. The shifts in the redox peaks with increasing iron content may be explained by considering the changes in the electronegativity of *M*, since the substitution of the Mn^{3+} by more electronegative Fe^{3+} could reduce the covalence of Mn—O below the $Mn^{3+}/^{4+}$ redox energy and increase the voltage of the $Mn^{3+}/^{4+}$ couple in $LiMn_{1-x}Fe_xPO_4(OH)$. Furthermore, the reduction in the overvoltage that accompanies Fe substitution may be attributed to facilitated diffusion of Li^+, which is caused by the local geometry change in the LiO_6 octahedral due to partial substitution of Mn^{3+} by Fe^{3+}. To better understand the detailed mechanism in charge–discharge, further structural studies are required to clarify the change in the crystal structure of $LiMn_{1-x}Fe_xPO_4(OH)$ during the electrochemical lithium (de)intercalation reaction.

4. Conclusions

Hydroxyphosphate solid solutions with a composition of $LiMn_{1-x}Fe_xPO_4(OH)$ ($0 \le x \le 0.3$) were synthesized and characterized structurally and electrochemically to assess their suitability as cathode materials for Li-ion batteries. SR-XRD data revealed that $LiMn_{1-x}Fe_xPO_4(OH)$ form continuous solid solutions, crystallizing in the triclinic *P*–1 space group for Fe contents between 0 and 0.3. The unit cell dimensions *a* and *b* decrease linearly and *c* increases linearly with increasing Fe content. Local geometric changes in $M^{3+}O_6$ and LiO_6 octahedra in the $LiMn_{1-x}Fe_xPO_4(OH)$ series are confirmed due to a decrease in the synergetic effect in the distortion by Jahn–Teller active Mn^{3+} ions and corner-shared interconnection with PO_4 tetrahedra and OH. Lithium-ion extraction and insertion in this tavorite-type $LiMn_{1-x}Fe_xPO_4(OH)$ is demonstrated and it exhibits an enhanced charge–discharge performance with a 30% increase in the capacity as the iron concentration increases from 0.0 to 0.3. The improved electrochemical properties and structural analysis results suggest that the local geometry change in crystal structure caused by partial substitution of Mn^{3+} by Fe^{3+} is correlated with the improved electrode performance of $LiMn_{1-x}Fe_xPO_4(OH)$.

Acknowledgements

This work was supported by a Grant-in-Aid for Scientific Research (A). The synchrotron radiation experiments were performed at the BL02B2 beam line at the SPring-8 facility with the approval of the Japan Synchrotron Radiation Research Institute (JASRI) (Proposal No. 2011A1612).

References

[1] A.K. Padhi, K.S. Nanjundaswamy, J.B. Goodenough, J. Electrochem. Soc. 144 (1997) 1188–1194.
[2] A.K. Padhi, K.S. Nanjundaswamy, C. Masquelier, S. Okada, J.B. Goodenough, J. Electrochem. Soc. 144 (1997) 1609–1613.
[3] A. Yamada, S.C. Chung, K. Hinokuma, J. Electrochem. Soc. 148 (2001) A224–A229.
[4] M.A.G. Aranda, J.P. Attfield, S. Bruque, Angew. Chem. Int. Ed. Engl. 31 (1992) 1090–1092.
[5] N. Marx, L. Croguennec, D. Carlier, E. Suard, A. Wattiaux, F. Le Cras, C. Delmas, Dalton Trans. 39 (2010) 5108–5116.
[6] Y. Yang, M. Hirayama, M. Yonemura, R. Kanno, J. Solid State Chem. (2012), doi:10.1016/j.jssc.2011.12.023, in press.
[7] A.R. Armstrong, P.G. Bruce, Nature 381 (1996) 499–500.
[8] Y.G. Zhang, L. Yi, S.Q. Fu, F. Guo, Bull. Chem. Soc. Jpn. 79 (2006) 270–275.
[9] T. Ishikawa, K. Tamasaku, M. Yabashi, Nucl. Instrum. Methods Phys. Res. Sec. A 547 (2005) 42–49.
[10] M.A.G. Aranda, J.P. Attfield, S. Bruque, F. Palacio, R.B.V. Dreele, J. Solid. State. Chem. 132 (1997) 202–212.
[11] F. Izumi, T. Ikeda, Mater. Sci. Forum 198 (2000) 321–324.
[12] H. Toraya, J. Appl. Crystallogr. 23 (1990) 485–491.
[13] D.R. Lide (Ed.), CRC Handbook of Chemistry and Physics, 82nd ed., CRC Press, Boca Raton, FL, 2001.
[14] Y. Song, P.Y. Zavalij, M. Suzuki, M.S. Whittingham, Inorg. Chem. 41 (2002) 5578–5786.